

**Search for Heavy Resonances Decaying to Tau Pairs with
the CMS Experiment**

by

A. A. Johnson

B.S., Carnegie Mellon University, 2011

M.S., University of Colorado, 2013

A thesis submitted to the
Faculty of the Graduate School of the
University of Colorado in partial fulfillment
of the requirements for the degree of
Doctor of Philosophy
Department of Physics
2016

This thesis entitled:
Search for Heavy Resonances Decaying to Tau Pairs with the CMS Experiment
written by A. A. Johnson
has been approved for the Department of Physics

Prof. John P. Cumalat

Prof. Kevin Stenson

Prof. Steven Wagner

Date _____

The final copy of this thesis has been examined by the signatories, and we find that both the content and the form meet acceptable presentation standards of scholarly work in the above mentioned discipline.

Johnson, A. A. (Ph.D., Physics)

Search for Heavy Resonances Decaying to Tau Pairs with the CMS Experiment

Thesis directed by Prof. John P. Cumalat

Two searches for heavy neutral resonances, Z' 's, decaying to back-to-back tau pairs are carried out using the Compact Muon Solenoid experiment at the Large Hadron Collider. The first, carried out during the 2012 data-taking run at $\sqrt{s} = 8$ TeV, focuses on the fully-leptonic channel, in which one tau decays to an electron and the other to a muon. The second, carried out during the 2015 run at $\sqrt{s} = 13$ TeV, focuses on the fully-hadronic channel, in which each tau decays to a hadronic jet. Each search employs a hybrid of background estimation strategies using both Monte Carlo simulation and data-driven methods. In both searches, observed data is found to be in agreement with Standard Model expectation and no excesses are observed. Limits are placed on the Z' , culminating in a world-record limit of 2.2 TeV at 95% confidence level.

Dedication

To my parents, Carl and Sharon Johnson. Without your constant love, support, and encouragement, none of this would have been remotely possible.

Acknowledgements

Here's where you acknowledge folks who helped. But keep it short, i.e., no more than one page, as required by the Grad School Specifications.

Contents

Chapter

1	Outline	1
1.1	Standard model	1
1.2	The CMS Experiment	1
1.3	EMu channel @ 8TeV	2
1.4	TauTau channel @ 13TeV	2
2	Introduction	3
2.1	Introduction	3
3	The Standard Model	5
4	The Compact Muon Solenoid (CMS) Experiment	7
4.1	The silicon tracker	9
4.1.1	The pixel detector	10
4.1.2	The strip tracker	10
4.2	The electromagnetic calorimeter	12
4.3	The hadronic calorimeter	12
4.4	The CMS magnet	15
4.5	The muon system	15
4.5.1	Drift tubes (DTs)	17

4.5.2	Cathode strip chambers (CSCs)	18
4.5.3	Resistive plate chambers (RPCs)	18
4.6	The trigger system	19
4.6.1	The Level-1 (L1) trigger)	19
4.6.2	The High level trigger (HLT)	20
4.7	Particle Reconstruction	20
4.7.1	Particle Flow	21
5	Strategy	26
6	Triggers	28
6.0.1	Single Lepton Trigger Efficiency	29
6.0.2	Single Electron Trigger Efficiency	29
6.0.3	Single Muon Trigger Efficiency	30
6.0.4	Di-Tau Trigger Efficiency	31
7	Data and Monte Carlo Samples	34
8	Physics Object Reconstruction	37
8.1	Jet Reconstruction	37
8.2	Electron Reconstruction and Identification	38
8.3	Muon Reconstruction and Identification	39
8.4	Tau Reconstruction and Identification	41
8.4.1	Efficiency of Tau Identification discriminators	43
8.4.2	Tau Energy Scale and Resolution	45
8.5	\cancel{E}_T	45
8.6	Corrections for Pile-Up	46

Appendix

Tables

Table

6.1	The trigger paths used to collected the data. Emulated trigger paths, in particular those most similar to the paths used to collect the data, are applied to the simulated samples.	28
6.2	Event rate in mu-tau control region after requiring denominator level selections	33
7.1	Collision Data Samples	34
7.2	MC Samples	36
8.1	Loose Jet-ID Selections.	38
8.2	Electron ID Selections.	40
8.3	μ Identification	41
8.4	Reconstructed Tau Decay Modes	42

Figures

Figure

4.1	The Large Hadron Collider located underneath the Franco-Swiss border at CERN near Geneva, Switzerland. The CMS Experiment is located on the French side in Cessy, France	8
4.2	The CMS Experiment (open for maintenance)	8
4.3	Schematic of the CMS Experiment showing the silicon trackers, electromagnetic calorimeter (ECAL), hadronic calorimeter (HCAL), superconducting solenoid, steel return yoke, and muon system.	9
4.4	Overview of the silicon tracker layout.	10
4.5	Diagram indicating the layout of the barrel pixel (BPIX) sensors (in green) and endcap pixel (FPIX) sensors (in pink)	11
4.6	Layout of the electromagnetic calorimeter (ECAL) indicating the configuration of the barrel (EB) and endcap (EE) crystals.	13
4.7	Layout of the hadronic calorimeter (HCAL) indicating the configuration of the barrel (HB) and endcap (HE) components as well as the outer HCAL (HO) lining the solenoid.	14
4.8	The superconducting solenoid.	16
4.9	Layout of the muon system highlighting the layered structure of the drift tubes (DTs, green), cathode strip chambers (CSCs, blue), and resistive plate chambers (RPCs, red).	17

6.1	The efficiency vs. p_T curves of the single-electron triggers used. Left column: barrel. Right column: endcap. The offline electron ID requirements used are HEEP (top row), MVANonTrig80 (middle row), MVATrigWP80 (bottom row).	30
6.2	The efficiency vs. p_T curves of the single-electron triggers used. Left column: barrel. Right column: endcap. The offline electron ID requirements used are HEEP (top row), MVANonTrig80 (middle row), MVATrigWP80 (bottom row). The two bins each contain half of the events with $p_T > 35$ GeV.	30
6.3	The efficiency vs. p_T curves of the single-muon triggers used. Left column: $ \eta < 1.2$. Right column: $ \eta > 1.2$. Bottom row: the two bins each contain half of the events with $p_T > 25$ GeV.	31
6.4	The per-leg τ_h trigger efficiency as a function of $p_T(\tau_h)$ for (a) simulated Z' signal sample on left (b) for data and all backgrounds obtained by requiring mu-tau region on right.	33
8.1	Decay Mode Finding efficiency as function of p_T , η , and number of vertices of generator-level taus	43
8.2	Efficiency of anti-muon discriminator (Loose3) as function of p_T , η , and number of vertices of generator-level taus	44
8.3	Efficiency of anti-electron discriminator (Loose/Medium MVA5) as function of p_T , η , and number of vertices of generator-level taus	44
8.4	Efficiency of isolation discriminator ("CombinedIsoDB3Hits") as function of p_T , η , and number of vertices of generator-level taus	44
8.5	Energy response of reconstructed taus, raw and vs. generated tau p_T	45

8.6 Distributions of the number of reconstructed primary vertices. Top: $e\mu$ channel.
Bottom: $e\tau_h$ channel. Left: before reweighting. Right: after reweighting (“official”
69 mb). The ratios after reweighting become flattest at an “unofficial” value of 71 mb.
The apparent substantial differences in the QCD “integrals” are artifacts of the
plotting procedure, in which bins with negative contributions are zero-ed. 46

Chapter 1

Outline

OUTLINE

1.1 Standard model

Z'

Why TauTau

Other BSM theories involving ditau pairs

1.2 The CMS Experiment

Pixels

Monitoring tool

Strips

ECAL

HCAL

Muon System

Triggering

L1 HLT

Computing @ CERN

1.3 EMu channel @ 8TeV

- MC samples used
- Generation methods
- Data samples used
- Object selection
- Validation
- Background estimation
- Lifetime cuts optimization
- Systematics
- Limit setting methodology impact of lifetime cuts on limit

1.4 TauTau channel @ 13TeV

- MC samples used
- Generation methods
- Data samples used
- Object selection
- Validation
- Background estimation
- Lifetime cuts optimization
- Systematics
- Limit setting methodology impact of lifetime cuts on limit
- The Standard Model

Chapter 2

Introduction

2.1 Introduction

The mission of particle physics is to increase our understanding of the most fundamental constituents of our universe and their interactions. These efforts have arguably been going on since the era of the Greek philosophers, who classified all matter into the elemental categories of earth, air, wind, and fire. As the centuries progressed, our knowledge of the nature of the universe has been refined as new theories were proposed to explain the phenomena we observe in nature, and, at the same time, more and more sophisticated experiments were designed to test them. Particle physics as a field today is broadly divided into two sub-fields: theory and experiment. Theorists seek to develop models that offer a more complete explanation of particle interactions, and experimentalists are tasked with validating these models. Efforts in particle theory in the late-20th century culminated in the Standard Model (SM) of particle physics, which has proven to be tremendously successful at describing a large number of observed particle phenomena (some which have been accurately validated to one part in ten billion!).

The SM is not without its deficiencies, however. Today, there remain many open questions in particle physics that are not sufficiently (or at all) addressed by the SM. To name just a few:

Why is there more matter than antimatter in the universe? What is dark matter? What is dark energy? Can the strong interaction be unified with the electroweak interaction? Why is the Higgs mass 125 GeV and not at the Planck scale?

Attempts to answer these questions require new theories modifying and building on the SM.

These theories must then be tested, which is where the experimentalists come in. While the SM was perhaps the crowning achievement of high energy theory in the twentieth century, the Large Hadron Collider (LHC) is arguably the most noteworthy undertaking in high energy experiment in the twenty-first. Located in Geneva, Switzerland at the European Organization for Nuclear Research (CERN, from the French “Conseil Europen pour la Recherche Nuclaire”), the LHC is the highest-energy particle collider ever built and has been an invaluable tool in the quest to validate theories of new physics.

This thesis presents an effort to use one of the primary experiments on the LHC, the Compact Muon Solenoid (CMS), to search for a new particle, called the Z' , predicted by many such “Beyond Standard Model” (BSM) theories. Part I will lay the groundwork, offering an overview of the SM and the modifying theories which predict the Z' ’s existence. Part II will discuss the tools used in the search: the LHC, the CMS experiment, and the substantial computing resources needed to conduct a full search for new physics. Part III will discuss the search during the 2012 data-taking run at the LHC, and Part IV will discuss the most recent search conducted during the 2015 run. Part V will offer an overview of future possibilities in this search effort as well as concluding remarks.

Part I

Chapter 3

The Standard Model

At the forefront of the interconnection between particle physics and cosmology are the following questions: (1) What is the origin of the matter-antimatter asymmetry?; (2) What is the origin of neutrino mass?; (3) Are there new fundamental forces in nature?; (4) What is the origin of dark energy; and (5) Is the Higgs boson solely responsible for electroweak symmetry breaking and the origin of mass? Much like the Higgs mechanism is introduced to account for the $SU(2)\times U(1)$ symmetry breaking, there are a plethora of theoretical models which incorporate additional gauge fields and interactions to address these questions. For example, string theory is considered a promising candidate for describing gravitational systems at strong coupling and thus plays a prominent role in the description of black holes and evolution of the universe through the understanding of the origin of dark energy. Similarly, models with additional neutrino fields at the TeV scale provide a possible explanation for the mass of light neutrinos. Such models often manifest themselves as new heavy particles that could be observed at the LHC. Surprisingly, some of these new particles predicted on the basis of pure particle physics arguments can even provide the correct dark matter relic density. There are several ways new heavy gauge bosons appear. The most natural possibility is one in which these heavy gauge bosons are the gauge field of a new local broken symmetry. Examples include models with a new $U(1)$ gauge symmetry, little Higgs models, and E6 Grand Unified Theories (GUT). In models with a new $U(1)$ gauge symmetry, the Z' is the gauge boson of the broken symmetry. In little Higgs models, breaking of the global symmetry by gauge and Yukawa interactions generates Higgs mass and couplings at the TeV scale that cancel off the SM

quadratic divergence of the Higgs mass from top, gauge, and Higgs loops. This results in one or more Z' bosons. In Kaluza-Klein models, the Z' bosons are excited states of a neutral, bulk gauge symmetry. From the breadth, scope, and implications of these models, it is apparent that probing these questions and puzzles potentially lies in the physics of new particles at the TeV scale.

Of particular interest for this analysis are models that include an extra neutral gauge boson that decays to pairs of high- $p_T \tau$ leptons. Although many models with extra gauge bosons obey the universality of the couplings, some models include generational dependent couplings resulting in extra neutral gauge bosons that preferentially decay to τ leptons, making this analysis an important mode for discovery. However, even if a new gauge boson decaying to $\mu\mu$ is discovered first, it will be critical to establish the $\tau\tau$ decay channel to establish the coupling relative to $\mu\mu$ channel. The Compact Muon Solenoid

Chapter 4

The Compact Muon Solenoid (CMS) Experiment

The CMS Experiment is a multipurpose particle detector located on the LHC ring underneath the Franco-Swiss border at CERN in Geneva, Switzerland. An overview of the experiments on the LHC ring can be seen in Figure 4.1. The experiment is located 100 meters underground in Cessy, France. CMS is 28.7 meters long, 15.0 meters in diameter, and weighs approximately 14,000 tonnes. It's arranged in a cylindrical, multi-layered structure consisting of a "barrel" and two endcaps, with the LHC beam passing through the vertical axis of the cylinder. CMS consists of several subdetectors, each designed to measure a different class or property of particle. From the beam line outward, the layers of CMS are the tracker, the electromagnetic calorimeter (ECAL), the hadronic calorimeter (HCAL), the superconducting solenoid, and the muon system (interspersed with the steel return yoke). A photograph of CMS can be seen in Figure 4.2.



Figure 4.1: The Large Hadron Collider located underneath the Franco-Swiss border at CERN near Geneva, Switzerland. The CMS Experiment is located on the French side in Cessy, France

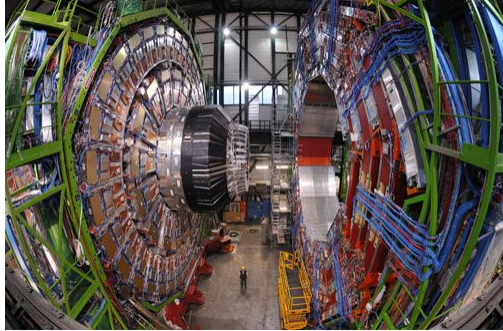


Figure 4.2: The CMS Experiment (open for maintenance)

The experiment uses a right-handed coordinate system: the origin is set at the pp collision point, with the x -axis pointing towards the center of the LHC ring, the y -axis pointing straight up, and the z -axis pointing along the beam line in the counter-clockwise direction. CMS also uses a pseudo-polar coordinate system, with θ defined as the polar angle from the beam axis, and η as the "pseudorapidity", itself defined as

$$\eta = -\ln [\tan (\theta/2)] \quad (4.1)$$

A diagram highlighting the layout of CMS can be seen in Figure 4.3.

4.1 The silicon tracker

The silicon tracker is the innermost detector element in CMS, and is designed to offer the highest resolution measurement of charged particle trajectories (such trajectories are referred to as "tracks"). The tracker is composed of approximately 200m^2 of silicon, and includes arrays of silicon pixels in the inner layer and arrays of silicon strips in the outer layer. The silicon elements are arranged in the densest configuration near to the interaction vertex ($r \approx 10\text{cm}$), with pixel size $\approx 100 \times 150\mu\text{m}^2$. As one moves away from the interaction vertex, the solid angle becomes large enough that the particle flux drops off to a degree that larger silicon elements may be used (silicon

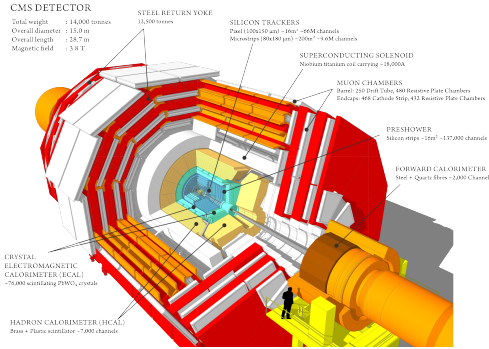


Figure 4.3: Schematic of the CMS Experiment showing the silicon trackers, electromagnetic calorimeter (ECAL), hadronic calorimeter (HCAL), superconducting solenoid, steel return yoke, and muon system.

strips measuring $10\text{cm} \times 80\mu\text{m}$ at $20\text{cm} < r < 55\text{cm}$, silicon strips measuring $25\text{cm} \times 180\mu\text{m}$ for $r > 55\text{cm}$. The total number of silicon elements is 66 million pixels and 9.6 million strips. The tracker is divided into a barrel segment and two forward endcaps. The endcaps contain two pixel and nine strip layers each, and the barrel segment is separated into an inner and outer barrel. A schematic of the tracker layout can be seen in Figure 4.4. Particle tracks are reconstructed from hits in the individual silicon pixels/strips, the track being interpolated between hits.

4.1.1 The pixel detector

The pixel detector, shown in Figure fig(PixelLayout), consists of three barrel layers and two endcap layers. The barrel has a length of 53 cm, and the endcap disks range from 6 cm to 15 cm in radius. The pixel modules are arranged in a ladder-like configuration in the barrel, with 768 total modules comprising the barrel. The endcap disks are arranged in a turbine-like fashion, with 24 "blades" per disk, and 7 pixel modules per blade for a total of 672 pixel modules in the endcaps. Each pixel consists of a readout chip (ROC), which are bump bonded to the modules. In total, the pixel detector includes about 16,000 ROCs.

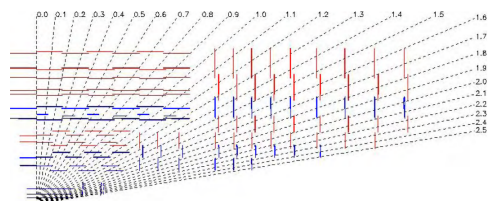


Figure 4.4: Overview of the silicon tracker layout.

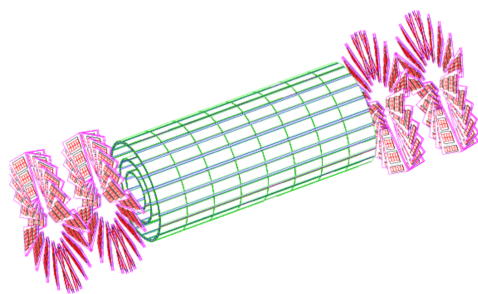


Figure 4.5: Diagram indicating the layout of the barrel pixel (BPIX) sensors (in green) and endcap pixel (FPIX) sensors (in pink)

4.1.2 The strip tracker

The strip tracker is divided into a barrel segment and two endcap segments. The barrel segment is itself divided into a Tracker Inner Barrel (TIB) section and a Tracker Outer Barrel (TOB) section. The TIB includes four layers of silicon strips each $320\mu\text{m}$ thick and ranging in pitch from $80\mu\text{m}$ and $120\mu\text{m}$. In the TOB, the lower rate of particle flux allows for larger strips (each $500\mu\text{m}$ thick and ranging in pitch from $120\mu\text{m}$ to $180\mu\text{m}$).

The endcaps are each comprised of a Tracker Endcap (TEC) and Tracker Inner Disks (TIDs). The TIDs are designed to fill the region between the TEC and the TIB. The TECs each contain nine disks, and each TID contains three disks. On each disk, the modules (for both TID and TEC) are arranged in rings centered on the beam line. The TID strips (and three innermost ring strips of the TEC) have thickness $320\mu\text{m}$, while the rest of the TEC strips have thickness $500\mu\text{m}$. In total the strip tracker contains about 15,400 strip modules.

4.2 The electromagnetic calorimeter

The next layer outward from the silicon tracker is the electromagnetic calorimeter (ECAL), which is designed primarily to measure energies of photons and electrons. The ECAL consists of an array of about 75,000 lead tungstate (PbWO_4) crystals, and has a barrel (BE) segment as well as two endcap (EE) segments. The BE segment has 61,200 crystals, while each EE segment contains 7,324 crystals.

PbWO_4 was chosen for the ECAL due to its short radiation length ($X_0 = 0.89\text{ cm}$), fast response time (80% of light emitted within 25ns), and radiation hardness (up to 10 Mrad).

The barrel (EB) crystals present an apparent cross-section (when viewed from the interaction vertex) of $\approx 22 \times 22\text{ mm}^2$, and are 230 mm (25.8 radiation lengths) thick. The barrel has an inner radius of 129 cm, and covers the pseudorapidity range $0 < |\eta| < 1.479$.

The endcap (EE) crystals are each arranged in two D-shaped semicircular aluminum plates. From these plates are cantilevered "supercrystal" structures consisting of 5x5 crystal blocks. Each

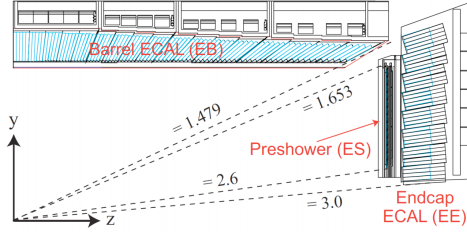


Figure 4.6: Layout of the electromagnetic calorimeter (ECAL) indicating the configuration of the barrel (EB) and endcap (EE) crystals.

crystal presents an apparent cross-section of $\approx 28.6 \times 28.6 \text{ mm}^2$, and are 220 mm (24.7 radiation lengths) thick, and the endcap crystals cover the pseudorapidity range $1.479 < |\eta| < 3.0$.

A diagram of the ECAL layout can be seen in Figure 4.6.

4.3 The hadronic calorimeter

Surrounding the ECAL is the hadronic calorimeter (HCAL). The primary function of the HCAL is to measure the energies of hadrons (particles made of quarks and gluons). Located just inside the solenoid magnet, the HCAL is primarily composed of brass panels made from melted-down artillery shells. Interspersed with the brass panels are plastic scintillation panels, in which are embedded wavelength-shifting (WLS) fibers, which carry the signal to clear fibers outside the scintillators for readout. As hadrons enter the HCAL, they produce secondary particles in the brass which in turn create further particles. These hadron "showers" then interact with the plastic scintillators, where the fibers carry the signal to hybrid photodiodes so the signal can be measured.

HCAL is divided into barrel (HB) and endcap (HE) portions. Due to limited space between the ECAL and solenoid, the HCAL also includes material outside the solenoid: the outer HCAL (HO) lining the solenoid, and the forward calorimeter (HF) outside the muon endcap system. These additions increase the total radiation lengths covered by the HCAL to 10.

While HB and HE use the brass-plastic configuration, HO uses the solenoid itself instead of the brass, although the same plastic scintillators are used. The HF uses steel in place of brass, and quartz fibers in place of plastic scintillators. This is done to preferentially select neutral

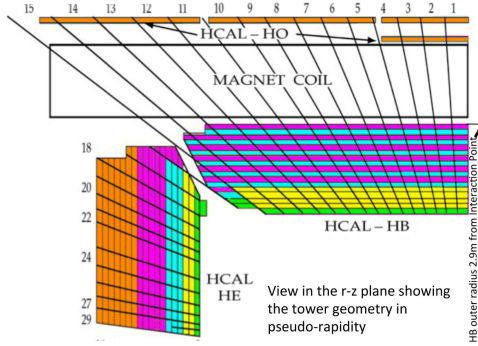


Figure 4.7: Layout of the hadronic calorimeter (HCAL) indicating the configuration of the barrel (HB) and endcap (HE) components as well as the outer HCAL (HO) lining the solenoid.

components of hadron showers, which are shorter and narrower and are thus well suited for the forward environment, which tends to be quite congested with particles.

A diagram of the HCAL layout is shown in Figure 4.7.

4.4 The CMS magnet

The need to measure high p_T muons has driven the requirements on the CMS magnetic field strength. With the goal to accurately determine both momentum and sign of 1TeV muons at $\Delta p/p \approx 10\%$, a superconducting solenoid with an interior magnetic field strength of 3.8T was chosen as the central design feature of CMS.

The solenoid is located outside the silicon tracker, ECAL, and HCAL systems but inside the muon system. Interspersed with the muon system is the steel return yoke, which contains the field outside the solenoid and provides a 2T field to allow the muon system to measure charged particle momentum.

To generate the magnetic field, 18,160 amperes are passed through four layers of tightly-wound superconducting Nb-Ti wire, resulting in a stored energy of 2.3 gigajoules.

The magnetic field generated by the solenoid bends charged particles according to the equation

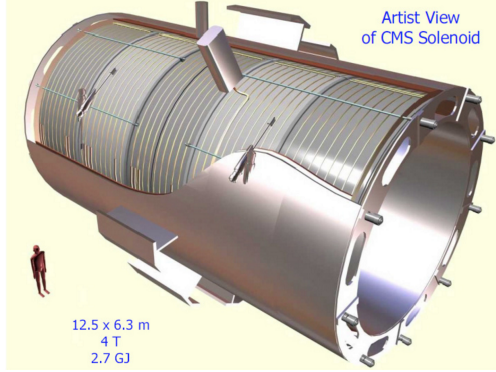


Figure 4.8: The superconducting solenoid.

$$R = \frac{p_T}{0.3eB}$$

where R is the radius of curvature (in meters), p_T is the transverse momentum (in GeV), e is the electron charge (in Coulombs), and B is the field strength (in Tesla). Thus, the transverse momentum (p_T) of the charged particle can be measured from the known field strength and the observed radius of curvature of the tracks measured in the tracker and muon systems.

An artist's rendition of the superconducting solenoid can be seen in Figure 4.8.

4.5 The muon system

The muon system is the outermost subdetector, and is central to the design of CMS. It is composed of three separate sensor elements: drift tubes (DTs), cathode strip chambers (CSCs), and resistive plate chambers (RPCs). A diagram of one quadrant of the muon system can be seen in Figure fig(muonSystemLayout). "MB" indicates the muon barrel subdetector, which is composed of DTs, "RB" indicates the RPC barrel subdetector, "ME" indicates the muon endcap subdetector (CSCs), and "RE" indicates the RPC endcap subdetector.

An overview of the layout of the muon system can be seen in Figure 4.9

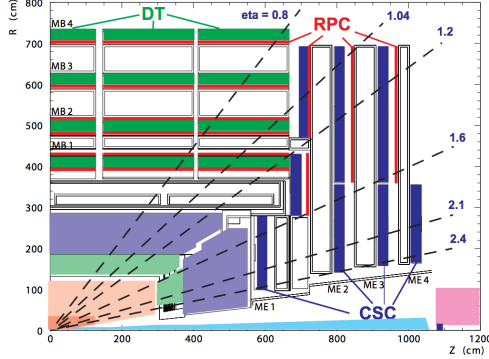


Figure 4.9: Layout of the muon system highlighting the layered structure of the drift tubes (DTs, green), cathode strip chambers (CSCs, blue), and resistive plate chambers (RPCs, red).

4.5.1 Drift tubes (DTs)

The barrel of the muon system contains 250 layers of DTs arranged in four layers (labeled MB1, MB2, MB3, and MB4 in Figure fig(muonSystemLayout)). In the MB1, MB2, and MB3 layers, DTs are arranged in 8 $r - \phi$ -measuring planes, and 4 z -measuring planes. The MB4 layer only contains $r - \phi$ -measuring planes.

Each DT is filled with a gaseous mixture of Argon (85%) and carbon dioxide (15%). Charged particles passing through the DT will ionize the gaseous mixture and produce a current along a central filament to be read out. The maximum drift length per DT is 2.0cm and the single point resolution is $\approx 200 \mu\text{m}$.

4.5.2 Cathode strip chambers (CSCs)

The muon endcap (ME) system is comprised of 234 CSCs in each endcap. The CSCs are trapezoidal in shape and are arranged in four layers (labeled ME1, ME2, ME3, and ME4 in Figure fig(muonSystemLayout)). The innermost layer (ME1), is made of 108 CSCs arranged in three rings of 36 CSCs each. The other layers each have two rings (18 CSCs on the inner ring, 36 on the outer ring, for a total of 54 CSCs per layer).

Each CSC is comprised of six gas gaps, with each gap containing a radial array of cathode strips and a plane of anode wires running perpendicular to the cathodes. The CSCs are overlapped

in ϕ to avoid gaps in the particle acceptance. When a charged particle ionizes the gas, it leaves a charge on the anode wire and an image charge on a group of cathode strips. The spatial resolution provided from each CSC is $\approx 200\mu\text{m}$.

The forward (endcap) region of the muon system can expect a higher muon flux, so CSCs were chosen due to their fast response time and fine resolution.

4.5.3 Resistive plate chambers (RPCs)

RPCs can be found in both the barrel and encaps of the muon system, and are used in parallel with the other two subsystems. The RPCs have timing resolution on the order of nanoseconds and are used primarily to resolve ambiguities in cases of multiple hits in the DTs or CSCs, thereby improving the overall accuracy of particle reconstruction.

There are two layers of RPCs "sandwiching" each of the first two DT layers (MB1 and MB2), while the outer DT layers (MB3 and MB4) are paired with one RPC each. The endcap CSCs are also paired with one RPC each.

Each RPC is comprised of parallel plates of bakelite enclosing two millimeter-thick gas gaps. Each gas gap contains a mixture of 96.2% R134a ($\text{C}_2\text{H}_2\text{F}_4$), 3.5% isobutane (C_4H_{10}), and 0.3% sulfur hexafluoride (SF_6).

4.6 The trigger system

When running at full luminosity, the LHC generates pp collisions at a rate of 40MHz. With each event requiring $\approx 10\text{MB}$ of digital storage space, this equates to a data-generation rate of 400TB per second. Since this is obviously unsustainable with current computer storage technology, CMS employs a trigger system to reduce the rate of stored events. Two levels of triggering are used: the hardware-based Level-1 (L1) trigger, which reduces the rate from 40MHz to approximately 100kHz, and the hardware-and-software-based High Level Trigger (HLT), which reduces the rate from $\approx 100\text{kHz}$ to 300Hz.

4.6.1 The Level-1 (L1) trigger)

The L1 trigger takes data from the muon system, HCAL, and ECAL in order to make a rapid decision about whether or not to keep the event and send it to the HLT for further review. The L1 triggering rate is about $3.2\mu\text{s}$, during which time the entirety of the data from the event is temporarily stored. Information from the silicon tracker is not used in this stage of triggering, as the time required by the tracker to reconstruct a track is outside this triggering time window.

The L1 trigger is divided into three major components: the calorimeter trigger, the muon trigger, and the global trigger. The calorimeter trigger looks at the combined (summed) energy deposits in ECAL and HCAL. If the sum is greater than a given threshold, an "accept" signal is sent to the global trigger. The muon trigger looks at the DTs, CSCs, and RPCs which in conjunction form the muon system. If they in concert report at least four muons, each having high transverse momentum and high-resolution tracks ("good"-quality muons), an "accept" signal is sent to the global trigger. The global trigger makes the final decision to reject the event or, if it has received "accept" signals from both the calorimeter trigger and muon trigger, to send it to the HLT.

4.6.2 The High level trigger (HLT)

The HLT is software-based and uses software-defined "HLT paths" in order to determine whether or not a given event will pass a particular physics object selection determined by the path. The advantage of this setup is that different HLT paths can be used by different analysis groups looking for different physics signatures.

The HLT first reconstructs the entirety of the event from the stored data passed to it by the L1 trigger, and determines whether the event passes a given trigger path. There are four broad categories of HLT path: electrons/photons and muons, jets, missing transverse energy (\cancel{E}_T), and taus. Hundreds of specific paths offering high levels of discrimination between required selection criteria are available and grouped into these four categories. As the paths are software-based and not hardware-based, new paths can be customized to the needs of any analysis effort.

In order to determine whether or not an event passes a given path, the entire event is reconstructed and run through three broad triggering steps: Stage 2 (calorimetry), Stage 2.5 (calorimetry+pixel hits), and Stage 3 (full reconstruction). In Stage 2, a threshold on calorimeter energy is applied. An object must have a combined ECAL+HCAL calorimetry energy greater than the threshold specified by the path in order to move on to Stage 2.5. In Stage 2.5, information from the pixel subdetector in the silicon tracker is used in order to verify that the hits recorded in the calorimetry towers have corresponding tracks in the pixel system (assuming the particle in question is charged). Finally, in Stage 3, information from the entire detector is used to reconstruct the entirety of objects in the event and ensure that they pass momentum, energy, and quality criteria specified by the path.

4.7 Particle Reconstruction

Even after a given event has passed the L1 trigger and HLT requirements, its constituent particles only exist as hit patterns in the various subdetectors of CMS. In order for any kind of meaningful physics analysis to be performed, these hit patterns must be turned into physics objects which are more easily-read by the CMS software framework (CMSSW). Broadly, the six principle objects that are "reconstructed" from raw detector data in this manner are: electrons, muons, taus, photons, jets, and missing energy (\cancel{E}_T). The chief set of software tools used to reconstruct physics objects is a group of algorithms collectively referred to as Particle Flow (PF).

4.7.1 Particle Flow

Particle Flow (PF) is the term used to refer to the general set of algorithms used to reconstruct physics objects (particles) out of raw detector data. The fundamental inputs to the PF algorithms are the charged particle tracks (from the silicon tracker), hits in the calorimetry towers (from ECAL and HCAL), and hits in the muon system. These fundamental inputs are then grouped into "blocks" which the PF algorithm translates into physics objects. Muons are identified by matching a track in the tracker with a hit in the muon system, charged hadrons are identified by matching

a track in the tracker with a hit in HCAL, and electrons are identified by matching a track in the tracker with a hit in ECAL. Photons and neutral hadrons leave no tracks, so they are identified as hits in ECAL and HCAL, respectively, with no matching tracks. As tracks are matched with calorimetry towers and muon hits, those hits are removed from consideration and whichever tower hits are leftover are assumed to be from photons or neutral hadrons. Once all the visible particles are reconstructed, conservation of momentum principles are applied to infer the missing energy, or E_T .

The following subsections will detail the methods used to reconstruct each class of particle, and a final subsection will detail the means by which the event data produced by Particle Flow is packaged into formats useful for analysis efforts.

4.7.1.1 Track reconstruction and vertexing

The goal of the silicon tracker is to reconstruct tracks indicating the trajectories of charged particles through the magnetic field, and furthermore to use these trajectories to “trace back” the origin of the particle, known as the vertex. The first vertex in each event, that corresponding to the pp collision, is known as the primary vertex (PV). The presence of multiple proton-proton collisions in each bunch crossing, a phenomenon known as pileup, presents the possibility of misidentifying the correct PV for a given event. Therefore, there is a need for a vertexing and tracking algorithms exhibiting a high degree of granularity.

To ensure this, tracks with the highest number of hits in the pixel and strip subsystems within the silicon tracker are recorded (and reconstructed) first. Tracks with three hits, high p_T , and close proximity to the beam spot are considered to be high quality. These tracks are reconstructed first, and their hits removed. For the remaining, lesser-quality tracks, looser criteria are applied iteratively until all tracker hits have been accounted for.

In order to determine the location of the PV, the reconstructed tracks are clustered together and the location is extrapolated by requiring that each track cluster share a plane compatible with the beam line. This is done online as well as offline so that the PV information can be relayed to

the HLT for use in the triggering process. The reconstruction algorithm uses only information from the pixel subdetector for the online reconstruction, while the offline reconstruction uses information from the entire tracker.

4.7.1.2 Electron reconstruction

Electrons are reconstructed via the combination of a track in the silicon tracker and hits in the ECAL towers. These tower hits are called “superclusters” and their size in η and ϕ is dictated by various clustering algorithms selected according to the relevant HLT path. As the electron interacts with the silicon in the tracker, it radiates photons via Bremsstrahlung. This emission causes the electron to bend further in the magnetic field. To account for this, the supercluster size is tuned to catch these Bremsstrahlung photons as well, thereby capturing the total energy of the electron before bending and leading to a more accurate calculation of the electron’s energy and momentum.

To fully reconstruct an electron track, one starts with a track **seed**, which is a possible electron trajectory found by interpolating between layer hits in the pixel and strip detectors. These track seeds must be cleaned and filtered in order to find the most likely track candidate, and then they must be matched with a supercluster in ECAL. There are two methods to achieve this. The first, ECAL driven seeding, begins by reconstructing superclusters in ECAL and attempts to match them with track seeds in the innermost layer of the pixel detector. The track is then reconstructed from these track seeds. The second, tracker driven seeding, begins with a high-quality track seed and attempts to match it to an appropriate supercluster in ECAL, while also taking into account other clusters arising from Bremsstrahlung photons. This is achieved by drawing straight lines tangent to the track towards the ECAL. If a corresponding cluster is found, it is added to the total energy of the electron.

4.7.1.3 Muon reconstruction

Muons can be measured both in the silicon tracker and the muon system. In order to reconstruct a muon, hits in the muon system (**stand-alone muons**) are matched to hits in the tracker in order to reconstruct a complete muon object, known as a **global muon**. These muons are reconstructed using two different methods, **global muon reconstruction (outside-in)** and **tracker muon reconstruction (inside-out)**.

Global muon reconstruction begins in the muon system. Hits in the DTs and CSCs are allocated into segments, which are short stubs containing just enough hits to assign each a momentum and direction vector. These segments are grouped together to form tracks in the muon system. These tracks, known as stand-alone muon tracks, are matched, one by one, with tracks from the tracker by comparing parameters of the two tracks propagated onto a common surface.

Tracker muon reconstruction begins in the silicon tracker. All tracks with $p_T > 0.5 \text{ GeV}/c$ and $p > 2.5 \text{ GeV}/c$ are considered possible muon candidates and are propagated outward toward the muon system, taking into account the magnetic field, expected energy loss, and the possibility for multiple Coulomb scattering in the detector material. If a hit in the muon system is found within 3 cm in local x, y coordinates, the candidate qualifies as a tracker muon.

Tracker muon reconstruction is more efficient than global muon reconstruction at low energies ($p < 5 \text{ GeV}/c$), since it only requires one muon segment in the muon system. Global muon reconstruction is more appropriate for muons with higher energies penetrating through more than one station in the muon system.

4.7.1.4 Photon and Neutral Hadron Reconstruction

Since photons and neutral hadrons are chargeless, and therefore leave no hits in the silicon tracker, the entirety of their reconstruction takes place in ECAL (photons) and HCAL (hadrons). The identification of photons and neutral hadrons takes place via so-called **clustering algorithms** which are designed to separate photons from neutral as well as charged hadrons, and to differen-

tiate photons originating from the primary or secondary decays from those generated by electrons undergoing Bremsstrahlung within ECAL.

Clustering algorithms involve three steps. First, a seed cluster is identified in one of the ECAL towers as a tower with a local energy maximum passing a threshold specified by the algorithm. Next, topological clusters are defined as clusters adjacent to (sharing at least one side in common with) the seed cluster and with cell energies passing another threshold. These thresholds are generally set to be two standard deviations above the base electronics noise level in each of the separate ECAL segments (80MeV in the barrel and 300MeV in the endcaps). Finally, topological clusters then generate as many “particle flow” clusters as there are seed clusters, and the energy in each particle flow cluster is allocated according to its distance from the seed.

Furthermore, in particle flow, ECAL/HCAL clusters are required **not** to match any tracks in the tracker in order to qualify as photon or neutral hadron candidates.

4.7.1.5 Jet Reconstruction

Jets are primarily reconstructed in ECAL and HCAL, although their charged constituents usually leave tracks in the silicon tracker as well. The majority of reconstructed jet energy comes from charged particles such as pions and kaons, and a smaller but still sizable portion comes from photons from π^0 decays in ECAL. Though numerous jet reconstruction algorithms exist, most jet candidates are reconstructed using the Particle Flow (PF) algorithm. The PF algorithm looks at the constituent particles in the jet: charged hadrons, neutral hadrons, and photons individually and then clusters them into jet candidates according to various clustering algorithms, the most common of which is the **anti- k_T** algorithm with a cone radius of $R = 0.5$. The energy of photons is determined from ECAL measurements, that of charged hadrons is measured with a combination of tracker, ECAL, and HCAL measurements, and the energy of neutral hadrons is measured according to the description in the previous section.

Approximately 90% of the reconstructed jet energy comes from charged hadrons and photons, while the remaining 10% comes from neutral hadrons. Since tracking information from the charged

hadrons is available, improved jet vertexing can be done and the impact of pileup can be mitigated.

Chapter 5

Strategy

A τ lepton is the heaviest known lepton with a mass of $1.777 \text{ GeV}/c^2$ and a lifetime of 2.9×10^{-13} seconds. Around one third of all τ leptons decay to e/μ , and the remainder decay into hadronic jets (τ_h). In the latter case, a τ_h consists of one, three, or (rarely) five charged mesons usually accompanied by one or more neutral pions.

We consider four distinct analyses for pairs of τ lepton decays, namely $e\mu$ (6.2%), $e\tau_h$ (23.1%), $\mu\tau_h$ (22.5%), and $\tau_h\tau_h$ (42%). We ignore the $Z' \rightarrow e^+e^-$ and $Z' \rightarrow \mu^+\mu^-$ channels due to the copious Drell-Yan $Z/\gamma^* \rightarrow e^+e^-$, $\mu^+\mu^-$ production, although there is ongoing development of algorithms to discriminate prompt e/μ from τ lepton decays to light leptons which will be utilized with the 2016 data/analysis.

The overall strategy of the analysis is similar in all channels. In general, we identify events with two oppositely charged, nearly back-to-back objects. Because the $\tau\tau$ system decays with up to four neutrinos, we expect to have missing transverse energy (\cancel{E}_T) present in the event. In contrast to Z' searches in the e^+e^- and $\mu^+\mu^-$ channels, the visible $\tau^+\tau^-$ mass does not produce a narrow peak due to the missing neutrinos. Instead, we look for a broad enhancement in the $\tau^+\tau^- + \cancel{E}_T$ invariant mass distribution consistent with new physics. Our selections maintain high efficiency for signal events, provide strong background suppression, and reduce the influence of systematic effects.

As $Z \rightarrow \tau^+\tau^-$ is both background as well as an important validation signal our final selection requirements are such that by removing or reversing just a few cuts we can obtain a clean sample

of $Z \rightarrow \tau^+\tau^-$ -events. In order to ensure robustness of the analysis and our confidence in the results, whenever possible we rely on the data itself to understand and validate the efficiency of reconstruction methods as well as the estimation of the background contributions. For that purpose we define control regions with most of the selections similar to what we use in our main search but enriched with events from background processes. Once a background enhanced region is created, we measure selection efficiencies in those regions and extrapolate to the region where we expect to observe our signal. In cases where a complete data–driven method is not possible we make use of scale factors, ratio between observed data events and expected MC events in the background enhanced region to estimate the background contribution in the signal region. Although each individual channel could have its own set of requirements, we maintain, wherever possible, consistent definitions and selection criteria between channels.

To quantify the significance of any possible excess or set upper limits on the production rate, we perform a fit of the $m(\tau_1, \tau_2, \cancel{E}_T)$ mass distribution and employ the CL_s technique to interpret the results in terms of the upper 95% credibility level limits for each channel. The joint limit is obtained by combining the posterior probability density functions (likelihood) and taking into account correlation of systematic uncertainties within and across channels.

The structure of this note is as follows: Sections 6 and 7 describes the data sets used in each analysis. Section 8 provides a brief discussion of the reconstruction and identification of the objects used to reconstruct our $\tau\tau$ pairs. Sections ??–?? describe the specific selections and background extraction methods applied to each individual channel. In Sections ??–?? we describe the statistical method used to extract the 95% C.L. upper limits and the results of the analysis.

Chapter 6

Triggers

For the semileptonic final states, we use single lepton triggers instead of $l \times \tau_h$ cross-triggers to maintain a similar strategy across channels and also allow us to use the τ_h isolation sidebands as control and validation samples. For the $e\mu$ final state, any trigger with iso-muon requirement, either a $e\mu$ cross-trigger or single-muon trigger, would eliminate the isolation sideband for QCD estimation. Hence, we use the same single-electron trigger as for the $e\tau_h$ final state. Trigger paths are summarized in Table 6.1. Note this constrains the object ID and phase space that we are studying. For example, the use of these triggers requires p_T cuts of 30 GeV, 35 GeV, and 60 GeV for our leading light leptons and τ_h 's in the $\mu\tau_h$, $e\tau_h$, and $\tau_h\tau_h$ channels, respectively.

Table 6.1: The trigger paths used to collect the data. Emulated trigger paths, in particular those most similar to the paths used to collect the data, are applied to the simulated samples.

Channel	Trigger Path
$\tau_h\tau_h$ (data RunC, sim)	HLT_DoubleMediumIsoPFTau40_Trk1_eta2p1_Reg
$\tau_h\tau_h$ (data RunD)	HLT_DoubleMediumIsoPFTau35_Trk1_eta2p1_Reg
$\mu\tau_h$ (data RunC)	HLT_IsoMu24_eta2p1
$\mu\tau_h$ (data RunD)	HLT_IsoMu18
$\mu\tau_h$ (sim)	HLT_IsoMu17 (L1 $\mu p_T > 18$ GeV)
$e\tau_h, e\mu$ (data)	HLT_Ele27_eta2p1_WPLoose
$e\tau_h, e\mu$ (sim)	HLT_Ele27_eta2p1_WP75

6.0.1 Single Lepton Trigger Efficiency

The single electron and muon trigger efficiencies are measured using a tag and probe method where we selected events with at least one electron and one muon pair satisfying the following requirements:

For electrons:

- $p_T > 13 \text{ GeV}$, $|\eta| < 2.1$, isolation < 0.15 , $d_{xy} < 0.045 \text{ cm}$, $d_z < 0.2 \text{ cm}$
- passing electron ID (we performed different measurements for "MVANonTrigWP80", "HEEP", "MVATrigWP80")
- no matched conversions
- number of missing hits = 0

For muons:

- $p_T > 20 \text{ GeV}$, $|\eta| < 2.1$, isolation < 0.15 , $d_{xy} < 0.045 \text{ cm}$, $d_z < 0.2 \text{ cm}$
- passing "Medium" muon ID

For the pair:

- $\Delta R(e\mu) > 0.3$
- choose the most isolated pair
- choose the opposite sign pair
- 3rd lepton veto

6.0.2 Single Electron Trigger Efficiency

To measure the single-electron trigger efficiency, after the preselection mentioned above, we select (tag) events with a single-muon trigger (HLT_IsoMu18 for data and HLT_IsoMu17_eta2p1

for MC with L1 $\mu p_T > 18$ GeV) with the offline muon matching the HLT muon that fired the trigger. Then, the trigger efficiency is defined at the fraction of events which also pass (probe) the single-electron trigger (HLT_Ele27_eta2p1_WPLoose for data and HLT_Ele27_eta2p1_WP75 for MC).

The efficiency curves of the single-electron triggers, measured vs. electron p_T , are shown in Figure 6.1. A $p_T > 35$ GeV cut is motivated to avoid the turn-on region. As shown in Figure 6.2, the efficiency curves were further binned into two p_T bins containing similar numbers of events. A weight of 0.94 is measured, and used in the analysis, as the ratio between simulated and observed events in which the selected electron is in the endcap region.

6.0.3 Single Muon Trigger Efficiency

To measure the single-muon trigger efficiency, after the preselection mentioned above, we select (tag) events with a single-electron trigger (HLT_Ele27_eta2p1_WPLoose for data and HLT_Ele27_eta2p1_WP75 for MC) with the offline electron match the HLT electron that fired the trigger. Then, the trigger efficiency is defined at the fraction of events which also pass (probe) the single-muon trigger (HLT_IsoMu18 for data and HLT_IsoMu17_eta2p1 for MC with L1 $\mu p_T > 18$ GeV).

The efficiency curves of the single-muon triggers, measured vs. muon p_T , are shown in Figure 6.3. A $p_T > 25$ GeV cut is motivated to avoid the turn-on region. As shown in lower two plots, the efficiency curves were further binned into two bins containing similar numbers of events. Weights of 0.991 and 0.986 are measured, and used in the analysis, as the ratios between simulated and observed events in which the selected muon $|\eta| \leq 1.2$ and $|\eta| > 1.2$.

6.0.4 Di-Tau Trigger Efficiency

The efficiency of the $\tau_h \tau_h$ trigger is measured using $Z \rightarrow \tau\tau \rightarrow \mu\tau_h$ events. The τ_h candidates reconstructed in the selected $Z \rightarrow \tau\tau \rightarrow \mu\tau_h$ events are required to pass the same τ_h identification used for the final analysis and which will be described in more detail in the sections to follow. The “denominator” selections used to define the $Z \rightarrow \tau\tau \rightarrow \mu\tau_h$ control sample are summarized below:

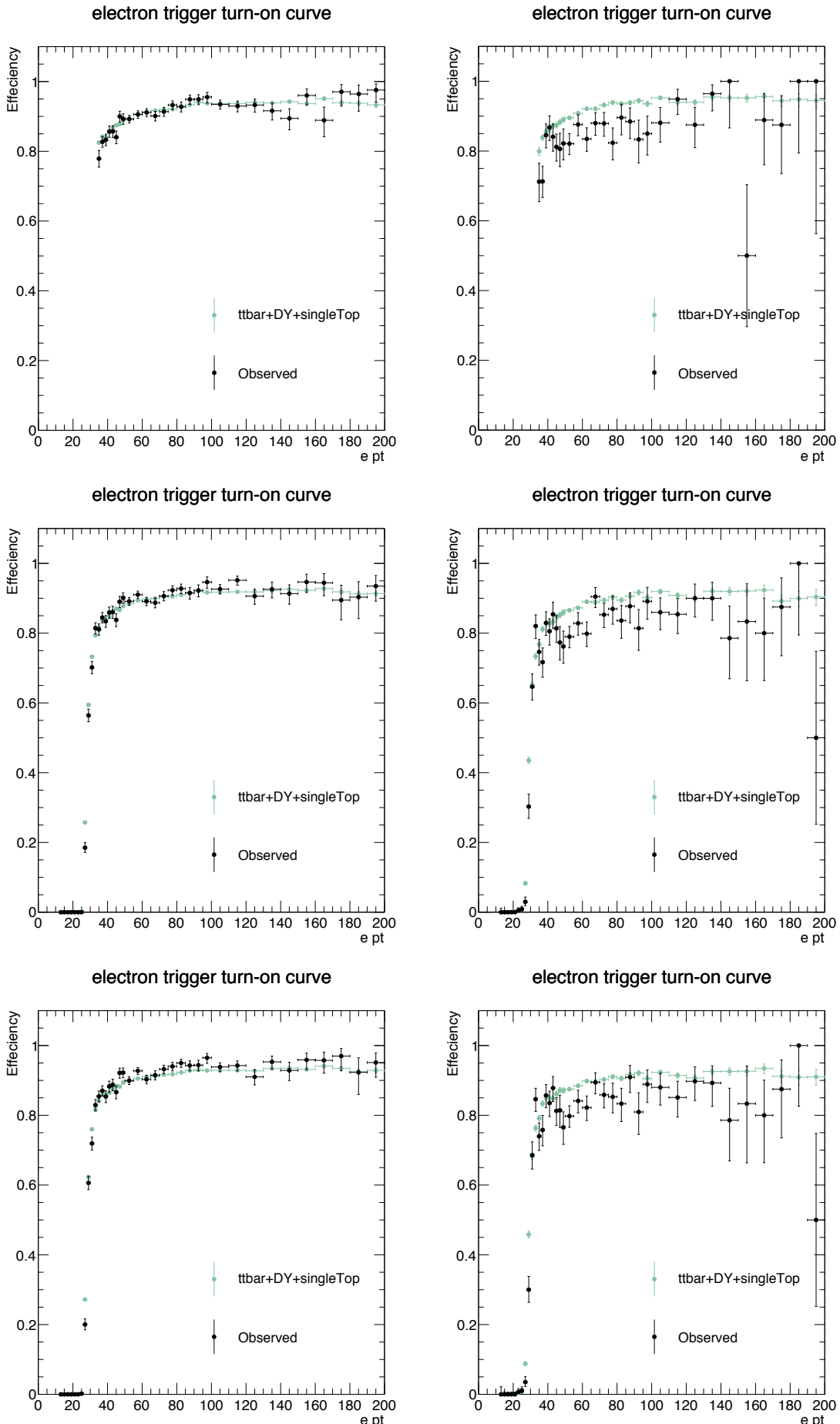


Figure 6.1: The efficiency vs. p_T curves of the single-electron triggers used. Left column: barrel.

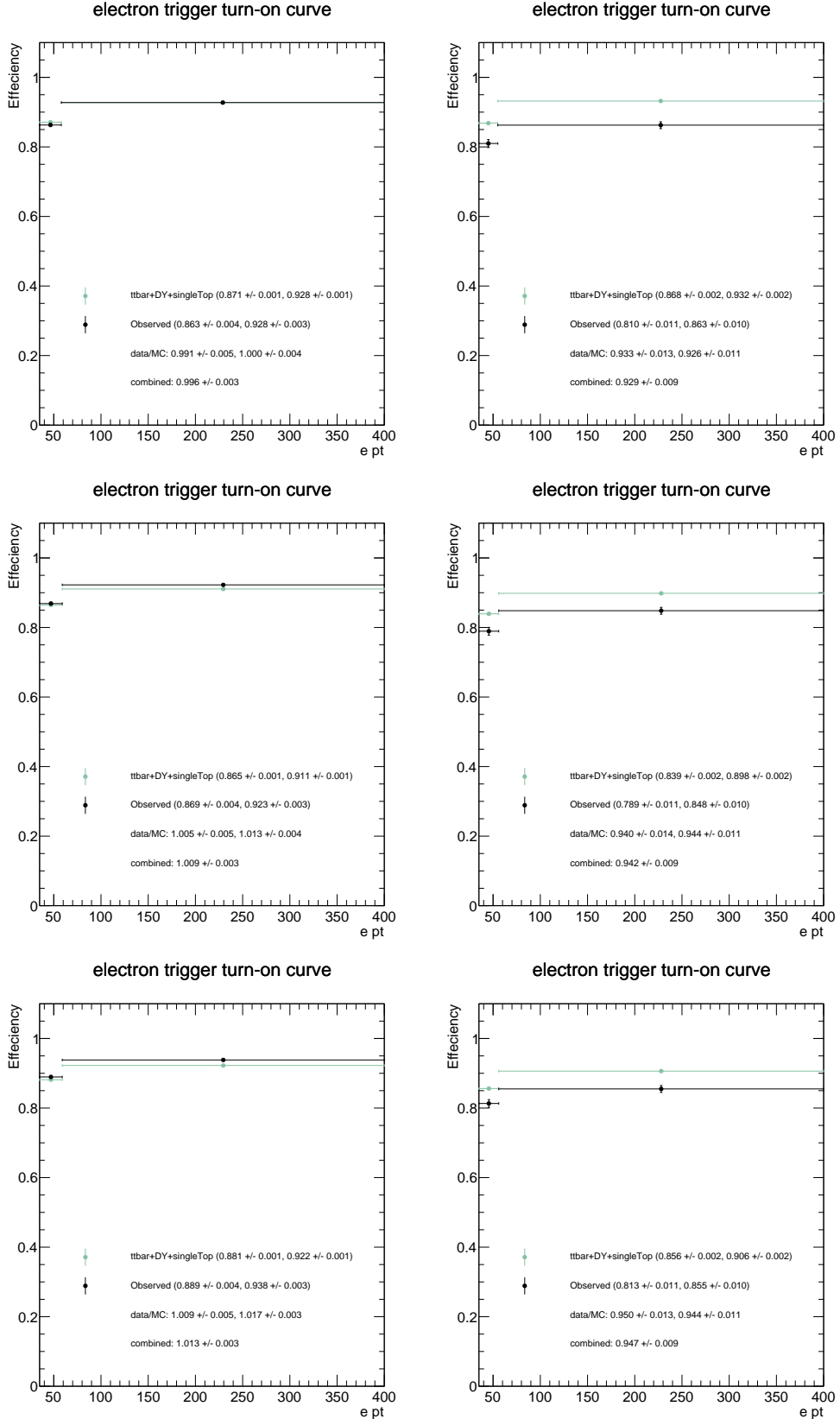


Figure 6.2: The efficiency vs. p_T curves of the single-electron triggers used. Left column: barrel. Right column: endcap. The offline electron ID requirements used are HEEP (top row), MVANonTrig80 (middle row), MVATrigWP80 (bottom row). The two bins each contain half of the events with $p_T > 35$ GeV.

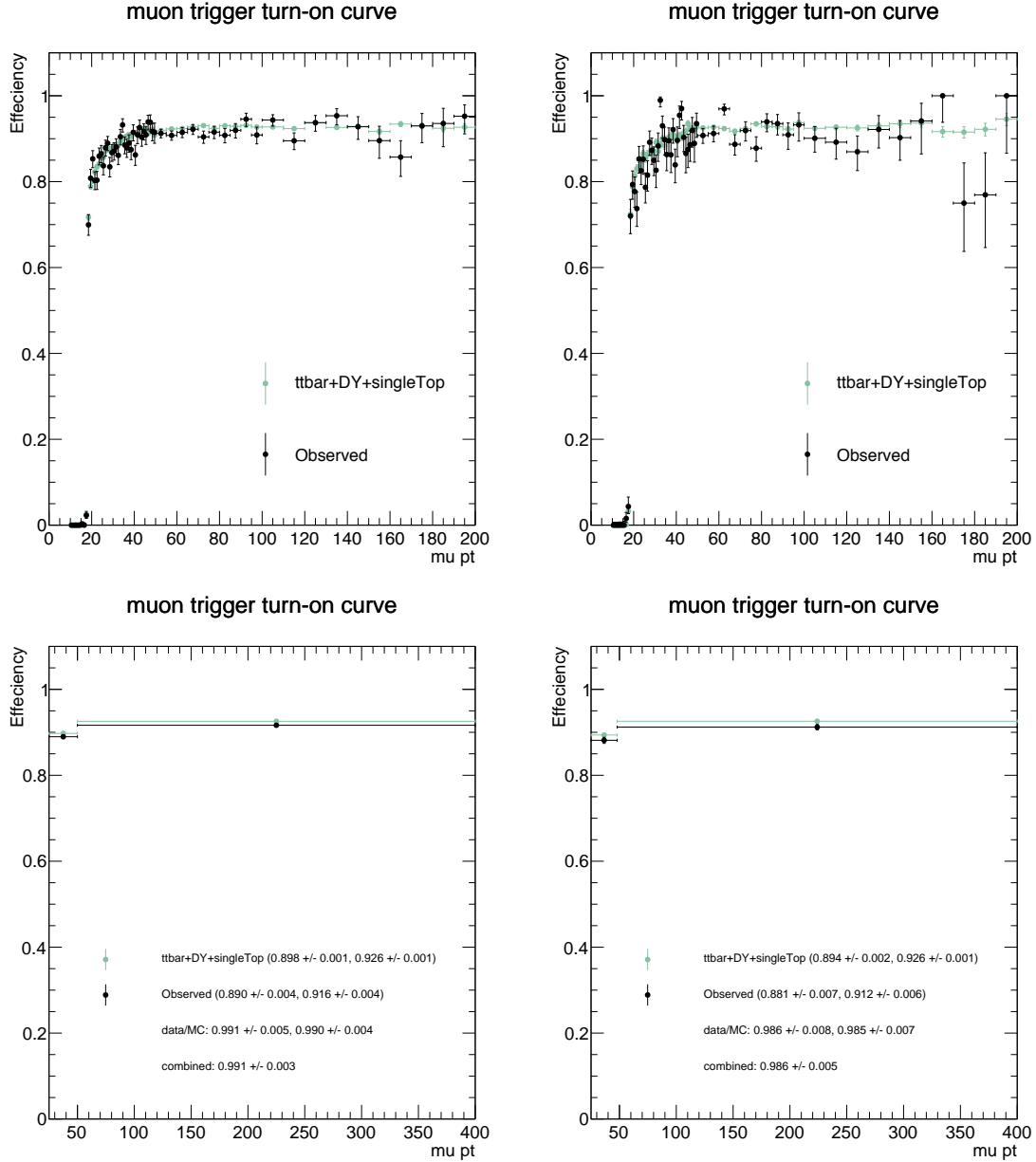


Figure 6.3: The efficiency vs. p_T curves of the single-muon triggers used. Left column: $|\eta| < 1.2$. Right column: $|\eta| > 1.2$. Bottom row: the two bins each contain half of the events with $p_T > 25$ GeV.

- Events must fire the HLT_IsoMu18 trigger (HLT_IsoMu17_eta2p1 with HLT pt cut of 18 GeV for MC)
- ≥ 1 global μ with $|\eta| < 2.1, p_T > 19$ GeV
- “isMediumMuon”
- muon best track $d_{xy} < 0.2$ cm , $d_z < 0.045$ cm w.r.t. PV
- Relative isolation (with $\delta\beta$ corrections) < 0.1
- ≥ 1 HPS τ_h with $|\eta| < 2.1, p_T > 20$ GeV
- Muon veto: “againstMuonTight3”
- Electron veto: “againstElectronVLooseMVA5”
- “old” decay mode finding
- Isolation: “byTightCombinedIsolationDeltaBetaCorr3Hits”
- $p_T > 5.$ GeV for leading Track of tau with $d_{xy} < 0.2$ cm and $d_z < 0.045$ cm w.r.t. PV
- $\Delta R(\mu, \tau_h) > 0.5$
- $Q(\mu) \times Q(\tau_h) < 0$
- $m_T(\mu, \cancel{E}_T) < 40$ GeV
- 0 jets tagged as b-jets
- 0 tagged electrons
- veto events with a second muon forming opposite-sign dimuon pair

The numerator is defined by additionally requiring those events to pass the HLT_IsoMu17_eta2p1_MediumIso trigger. The efficiency is measured for each τ_h leg individually and parametrized as function of p_T (Figure 6.4). From the plot it is clear that the emulation of the trigger in simulation does not

provide the correct trigger efficiency observed in data. This is mainly due to a difference in the trigger definition in MC, specifically the L1 seed. Therefore, we do not apply the trigger in MC, but instead model the correct per leg trigger efficiency observed in data by weighing the predictions from simulation using the fit of the trigger efficiency curve in data (black solid curve in the plot). The trigger efficiency at the plateau is approximately 90%.

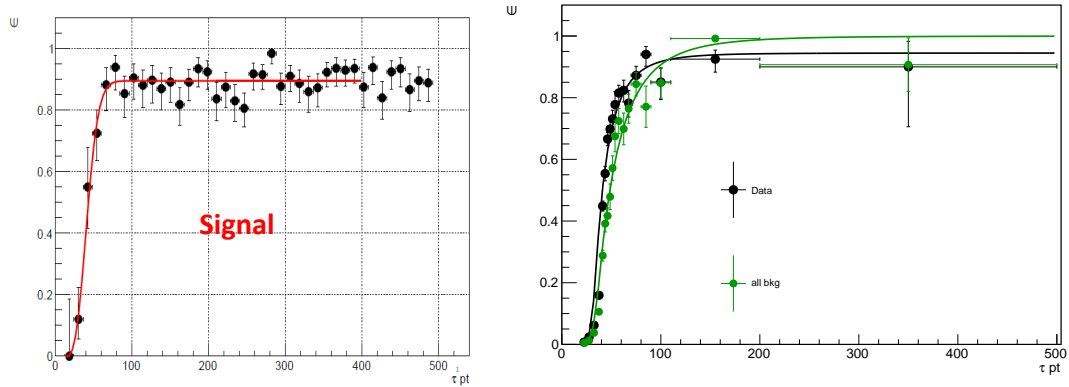


Figure 6.4: The per-leg τ_h trigger efficiency as a function of $p_T(\tau_h)$ for (a) simulated Z' signal sample on left (b) for data and all backgrounds obtained by requiring mu-tau region on right.

Figure 6.4 (right) shows the trigger efficiency for data and all backgrounds obtained by requiring $Z \rightarrow \tau_\mu \tau_h$. Most of the backgrounds are taken from simulation except QCD whose shape and rate have been taken from same sign control region from data by subtracting the contribution of other backgrounds. QCD normalization is then corrected by OS/LS ratio which is taken as ~ 1.05 . Table 6.2 shows the event yield in this control region requiring the denominator selections. The “purity”, fraction of DYJets events out of all backgrounds, of this region comes out to be $\sim 65\text{-}66\%$. The efficiency curves on Figure 6.4 (right) is fitted with crystall-ball function.

Table 6.2: Event rate in mu-tau control region after requiring denominator level selections

Sample	Events
Data	19578
$t \bar{t}$	170.881 ± 13.072
W+Jets	2127.76 ± 46.128
Z+Jets	12218.5 ± 110.544
QCD	4003.93 ± 63.277

Chapter 7

Data and Monte Carlo Samples

The 13 TeV collision data collected by the CMS detector in year 2015 is used in this analysis.

Table 7.1 shows the collision datasets used. The official JSON file is used to select “good” run ranges and lumi sections. The total integrated luminosity of the collision data samples is 2.11 fb^{-1} .

The official Spring miniAODv2 2015 MC samples are used for all Standard Model processes. The leading order generators, PYTHIA8 and MADGRAPH, were mainly used for Signal and Background MC production. The predicted background yields in simulation were determined using NLO or NNLO cross-sections, while the signal yields and distributions in all plots shown in this AN were normalized using the leading order cross-sections shown in Table 7.2. Table 7.2 shows the entire list of the MC samples used for this analysis.

Table 7.1: Collision Data Samples

Physics Sample	Official CMS Datasets
Run 2015C SingleMu 05 Oct ReMiniAOD	<i>/SingleMuon/Run2015C_25ns-05Oct2015-v1/MINIAOD</i>
Run 2015D SingleMu 05 Oct ReMiniAOD	<i>/SingleMuon/Run2015D-05Oct2015-v1/MINIAOD</i>
Run 2012D SingleMu PromptReco v4	<i>/SingleMuon/Run2015D-PromptReco-v4/MINIAOD</i>
Run 2015C SingleElectron 05 Oct ReMiniAOD	<i>/SingleMuon/Run2015C_25ns-05Oct2015-v1/MINIAOD</i>
Run 2015D SingleElectron 05 Oct ReMiniAOD	<i>/SingleElectron/Run2015D-05Oct2015-v1/MINIAOD</i>
Run 2012D SingleElectron PromptReco v4	<i>/SingleElectron/Run2015D-PromptReco-v4/MINIAOD</i>
Run 2015C Tau 05 Oct ReMiniAOD	<i>/Tau/Run2015C_25ns-05Oct2015-v1/MINIAOD</i>
Run 2015D Tau 05 Oct ReMiniAOD	<i>/Tau/Run2015D-05Oct2015-v1/MINIAOD</i>
Run 2012D Tau PromptReco v4	<i>/Tau/Run2015D-PromptReco-v4/MINIAOD</i>

Because the MC simulated samples contain a pileup (PU) distribution that does not match that of data, the MC needs to be properly weighted to fit the PU distribution observed in data. The

reweighting of MC events is performed by determining the probabilities to obtain n interactions in data ($P_{data}(n)$) and MC ($P_{MC}(n)$) and using the event weights

$$w_{PU}(n) = \frac{P_{data}(n)}{P_{MC}(n)} \quad (7.1)$$

to reweigh MC events based on the number of interactions. The recommended minbias cross-section of 69 mb is used to determine these weights.

Table 7.2: MC Samples

Process	cross-section (pb)	Official CMS Datasets (MINIAODSIM)
$Z \rightarrow ll$	6025.2	$/DYJetsToLL_M-50_TuneCUETP8M1_13TeV-madgraphMLM-pythia8/RunII Spring15 MiniAO Dv2-74X_mc Run2_asymptotic_v2-v1$
HT binned LO samples	147.4*1.23 40.99*1.23 5.678*1.23 2.198*1.23	$/DYJetsToLL_M-50_HT-100 to 200_TuneCUETP8M1_13TeV-madgraphMLM-pythia8/RunII Spring15 MiniAO Dv2-74X_mc Run2_asymptotic_v2-v1/$ $/DYJetsToLL_M-50_HT-200 to 400_TuneCUETP8M1_13TeV-madgraphMLM-pythia8/RunII Spring15 MiniAO Dv2-74X_mc Run2_asymptotic_v2-v1$ $/DYJetsToLL_M-50_HT-400 to 600_TuneCUETP8M1_13TeV-madgraphMLM-pythia8/RunII Spring15 MiniAO Dv2-74X_mc Run2_asymptotic_v2-v1$ $/DYJetsToLL_M-50_HT-600 to Inf_TuneCUETP8M1_13TeV-madgraphMLM-pythia8/RunII Spring15 MiniAO Dv2-74X_mc Run2_asymptotic_v2-v1$
$Z \rightarrow ll$ mass binned NLO samples	6025.2 7.67*0.987 0.423*0.987 0.24*0.987 0.035*0.987 0.03*0.987 0.016*0.987	$/DYJetsToLL_M-50_TuneCUETP8M1_13TeV-amcatnloFXFX-pythia8/RunII Spring15 MiniAO Dv2-74X_mc Run2_asymptotic_v2-v1$ $/DYJetsToLL_M-200 to 400_TuneCUETP8M1_13TeV-amcatnloFXFX-pythia8/RunII Spring15 MiniAO Dv2-74X_mc Run2_asymptotic_v2-v1$ $/DYJetsToLL_M-400 to 500_TuneCUETP8M1_13TeV-amcatnloFXFX-pythia8/RunII Spring15 MiniAO Dv2-74X_mc Run2_asymptotic_v2-v1$ $/DYJetsToLL_M-500 to 700_TuneCUETP8M1_13TeV-amcatnloFXFX-pythia8/RunII Spring15 MiniAO Dv2-74X_mc Run2_asymptotic_v2-v3$ $/DYJetsToLL_M-700 to 800_TuneCUETP8M1_13TeV-amcatnloFXFX-pythia8/RunII Spring15 MiniAO Dv2-74X_mc Run2_asymptotic_v2-v1$ $/DYJetsToLL_M-800 to 1000_TuneCUETP8M1_13TeV-amcatnloFXFX-pythia8/RunII Spring15 MiniAO Dv2-74X_mc Run2_asymptotic_v2-v1$ $/DYJetsToLL_M-1000 to 1500_TuneCUETP8M1_13TeV-amcatnloFXFX-pythia8/RunII Spring15 MiniAO Dv2-Asymp25ns_74X_mc Run2_asymptotic_v2-v1$
$W + jets$ HT binned LO samples	61526.7 1345*1.21 359.7*1.21 48.91*1.21 18.77*1.21	$/WJetsToLNu_TuneCUETP8M1_13TeV-madgraphMLM-pythia8/RunII Spring15 MiniAO Dv2-74X_mc Run2_asymptotic_v2-v1$ $/WJetsToLNu_HT-100 To 200_TuneCUETP8M1_13TeV-madgraphMLM-pythia8/RunII Spring15 MiniAO Dv2-74X_mc Run2_asymptotic_v2-v1$ $/WJetsToLNu_HT-200 To 400_TuneCUETP8M1_13TeV-madgraphMLM-pythia8/RunII Spring15 MiniAO Dv2-74X_mc Run2_asymptotic_v2-v1$ $/WJetsToLNu_HT-400 To 600_TuneCUETP8M1_13TeV-madgraphMLM-pythia8/RunII Spring15 MiniAO Dv2-74X_mc Run2_asymptotic_v2-v1$ $/WJetsToLNu_HT-600 to Inf_TuneCUETP8M1_13TeV-madgraphMLM-pythia8/RunII Spring15 MiniAO Dv2-74X_mc Run2_asymptotic_v2-v1$
$t\bar{t}$ single Top samples	831.76 35.6 35.6 136.02*0.108*3 80.95*0.108*3	$/TT_TuneCUETP8M1_13TeV-powheg-pythia8/RunII Spring15 MiniAO Dv2-74X_mc Run2_asymptotic_v2_ext3-v1$ $/ST_tW_antitop_5f_inclusiveDecays_13TeV-powheg-pythia8_TuneCUETP8M1/RunII Spring15 MiniAO Dv2-74X_mc Run2_asymptotic_v2-v1$ $/ST_tW_top_5f_inclusiveDecays_13TeV-powheg-pythia8_TuneCUETP8M1/RunII Spring15 MiniAO Dv2-74X_mc Run2_asymptotic_v2-v1$ $/ST_t-channel_top_4f_leptonDecays_13TeV-powheg-pythia8_TuneCUETP8M1/RunII Spring15 MiniAO Dv2-74X_mc Run2_asymptotic_v2-v1$ $/ST_t-channel_antitop_4f_leptonDecays_13TeV-powheg-pythia8_TuneCUETP8M1/RunII Spring15 MiniAO Dv2-74X_mc Run2_asymptotic_v2-v1$
VV $ZZ \rightarrow 2l2q$ $ZZ \rightarrow 4l$ $WW \rightarrow lr2q$ $WZ \rightarrow 2l2q$ $WZ + jets$ $WZ \rightarrow l3\nu$ $WZ \rightarrow lr2q$	11.95 3.22 1.212 49.997 5.595 5.26 3.05 10.71	$/VVToL2Nu_13TeV_amcatnloFXFX_madspin_pythia8/RunII Spring15 MiniAO Dv2-74X_mc Run2_asymptotic_v2-v1$ $/ZZTo2L2Q_13TeV_amcatnloFXFX_madspin_pythia8/RunII Spring15 MiniAO Dv2-74X_mc Run2_asymptotic_v2-v1$ $/ZZTo4L_13TeV_amcatnloFXFX_pythia8/RunII Spring15 MiniAO Dv2-74X_mc Run2_asymptotic_v2-v1$ $/WWTo1L1Nu2Q_13TeV_amcatnloFXFX_madspin_pythia8/RunII Spring15 MiniAO Dv2-74X_mc Run2_asymptotic_v2-v1$ $/WZTo2L2Q_13TeV_amcatnloFXFX_madspin_pythia8/RunII Spring15 MiniAO Dv2-74X_mc Run2_asymptotic_v2-v1$ $/WZJets_TuneCUETP8M1_13TeV-amcatnloFXFX_pythia8/RunII Spring15 MiniAO Dv2-74X_mc Run2_asymptotic_v2-v1$ $/WZTo1L3Nu_13TeV_amcatnloFXFX_madspin_pythia8/RunII Spring15 MiniAO Dv2-74X_mc Run2_asymptotic_v2-v1$ $/WZTo1L1Nu2Q_13TeV_amcatnloFXFX_madspin_pythia8/RunII Spring15 MiniAO Dv2-74X_mc Run2_asymptotic_v2-v1$
QCD samples	720648000	$/QCD_Pt200 to Inf_MuEnrichedPt15_TuneCUETP8M1_13TeV_pythia8/RunII Spring15 MiniAO Dv2-74X_mc Run2_asymptotic_v2-v1$
$Z'(500)$ $Z'(1000)$ $Z'(1500)$ $Z'(2000)$ $Z'(2500)$ $Z'(3000)$	9.33 0.468 0.0723 0.0173 0.00554 0.00129	$/ZprimeToTauTau_M_500_TuneCUETP8M1_tauola_13TeV_pythia8/RunII Spring15 MiniAO Dv2-74X_mc Run2_asymptotic_v2-v1$ $/ZprimeToTauTau_M_1000_TuneCUETP8M1_tauola_13TeV_pythia8/RunII Spring15 MiniAO Dv2-74X_mc Run2_asymptotic_v2-v1$ $/ZprimeToTauTau_M_1500_TuneCUETP8M1_tauola_13TeV_pythia8/RunII Spring15 MiniAO Dv2-74X_mc Run2_asymptotic_v2-v1$ $/ZprimeToTauTau_M_2000_TuneCUETP8M1_tauola_13TeV_pythia8/RunII Spring15 MiniAO Dv2-74X_mc Run2_asymptotic_v2-v1$ $/ZprimeToTauTau_M_2500_TuneCUETP8M1_tauola_13TeV_pythia8/RunII Spring15 MiniAO Dv2-74X_mc Run2_asymptotic_v2-v1$ $/ZprimeToTauTau_M_3000_TuneCUETP8M1_tauola_13TeV_pythia8/RunII Spring15 MiniAO Dv2-74X_mc Run2_asymptotic_v2-v1$

Chapter 8

Physics Object Reconstruction

8.1 Jet Reconstruction

Particle-flow (PF) technique [?, ?] is used to improve the jet p_T and angular resolution in this analysis. The PF technique combines information from different subdetectors to produce a mutually exclusive collection of particles (namely muons, electrons, photons, charged hadrons and neutral hadrons) that are used as input for the jet clustering algorithms. Jets are clustered using the anti- k_T algorithm [?], with a distance parameter of $R = 0.4$ in $\eta\text{-}\phi$ plane (defined as $\Delta R = \sqrt{\Delta\eta^2 + \Delta\phi^2}$) by summing the four-momenta of individual PF particles.

The jets require energy corrections obtained using simulated events that are generated with **PYTHIA**, processed through a detector simulation based on **GEANT4**, and confirmed with in situ measurements of the p_T balance. The overall jet-energy corrections depend on the η and p_T values of jets. The jet-energy corrections are applied by L1 FastJet, L2 Relative, and L3 Absolute corrections. In order to remove the extra energy in jets from underlying event (UE) and pileup (PU), the L1 FastJet corrections use the event-by-event UE/PU densities. The L2 and L3 corrections use jet balancing and photon+jet events to improve and provide a better energy response as a function of jet p_T and η . For data, additional residual corrections are applied.

Jets are required to have $p_T > 30$ GeV and $|\eta| < 2.4$. For the identification of jets the loose PF ID is used in this analysis. Table 4 shows the selection criteria used for the recommended loose PF ID, which are validated in other studies [?]. The jet reconstruction and ID efficiency in simulation is >98%.

Table 8.1: Loose Jet-ID Selections.

Selection	Cut
Neutral Hadron Fraction	< 0.99
Neutral EM Fraction	< 0.99
Number of Constituents	> 1
And for $\eta < 2.4$, $\eta > -2.4$ in addition apply	
Charged Hadron Fraction	> 0
Charged Multiplicity	> 0
Charged EM Fraction	< 0.99

8.1.0.1 b-Jet Tagging

In this analysis, b-tagged jets are used for two purposes: to reduce $t\bar{t}$ background in the signal region and to obtain $t\bar{t}$ enriched control samples used to estimate the signal rate.

The CSVv2 algorithm [?] is used to identify jet as originating from hadronization of a b-quark. This algorithm combines reconstructed secondary vertex and track-based lifetime information to build a likelihood-based discriminator to distinguish between jets from b-quarks and those from charm or light quarks and gluons.

The minimum thresholds on these discriminators define loose, medium, and tight operating points with a misidentification probability of about 10%, 1%, and 0.1%, respectively, with an average jet p_T of about 80 GeV. The loose operating point for an efficiency about 85% is used in this analysis. A large sample of pair-produced top quark events is used to measure b-tagging efficiency using several methods [?]. A scale factor is applied to correct for differences in b-tagging efficiency between data and simulation [?].

8.2 Electron Reconstruction and Identification

Electrons are reconstructed using information from the tracker and Ecal detectors. Electrons passing through the silicon tracker material lose energy due to Bremsstrahlung radiation. The energy of the radiated photons is spread over several crystals of the Ecal detector along the electron trajectory, mostly in the ϕ direction (the magnetic field is in the z direction). Two algorithms based

on energy clustering, “Hybrid” for the barrel and “Island” for the endcaps, are used to measure the energy of electrons and photons [?].

Electron tracks are reconstructed by matching trajectories in the silicon strip tracker to seed hits in the pixel detector. A pixel seed is composed of two pixel hits compatible with the beam spot. A Gaussian Sum Filter (GSF) is used for the reconstruction of trajectories in the silicon strips. In order to minimize the many possible trajectories due to different combinations of hits, the track that best matches an energy supercluster in the Ecal is chosen to be the reconstructed track.

The preselection of primary electron candidates requires good geometrical matching and good agreement between the momentum of the track and the energy of the ECAL supercluster. Two quantities used to estimate the geometrical matching are $\Delta\eta_{in} = \eta_{sc} - \eta_{vertex}^{Track}$ and $\Delta\phi_{in} = \phi_{sc} - \phi_{vertex}^{Track}$. The η_{sc} and ϕ_{sc} coordinates correspond to the supercluster position and are measured using an energy weighted algorithm. The η_{vertex}^{Track} and ϕ_{vertex}^{Track} coordinates are the position of the track at the interaction vertex extrapolated, as a perfect helix, to the Ecal detector. The good energy-momentum matching is measured by taking the ratio between the corrected energy E_{corr} in the Ecal supercluster and the momentum of the track P_{in} measured in the inner layers of the tracker.

Electron selections have two main components, electron identification (eID) and electron isolation. In this analysis we use the non-triggering MVA electron identification. The MVA cuts used to define the 80% and 90% signal efficiency working points are summarized in Table 8.2. In all channels, the identification and isolation used follows the POG recommended criteria. The exact discriminator names and working points for each channel are listed and described in their respective sections.

8.3 Muon Reconstruction and Identification

Muon reconstruction is a multistep process that begins with the information gathered from the muon subdetector. As a first step, standalone muons are reconstructed from hits in the individ-

Table 8.2: Electron ID Selections.

Category	MVA _{min cut} (80% signal eff)	MVA _{min cut} (90% signal eff)
Barrel ($\eta < 0.8$) p_T 5–10	0.287435	-0.083313
Barrel ($\eta > 0.8$) p_T 5–10	0.221846	-0.235222
Endcap p_T 5–10	-0.303263	-0.67099
Barrel ($\eta < 0.8$) $p_T > 10$	0.967083	0.913286
Barrel ($\eta > 0.8$) $p_T > 10$	0.929117	0.805013
Endcap $p_T > 10$	0.726311	0.358969

ual drift tube (DT) and cathode strip (CSC) chambers. Hits from the innermost muon stations are combined with hits in the other muon segments using the Kalman fitting technique. The standalone muon trajectory is reconstructed by extrapolating from the innermost muon station to the outer tracker surface. This standalone trajectory is then used to find a matching track reconstructed in the inner silicon tracker. Finally, standalone muons and matching silicon tracks are used to perform a global fit resulting in a “global” muon. Muon reconstruction is described in more detail in [?].

Global muons are reconstructed by combining tracker muons from the inner silicon tracker and standalone muons from the muon chambers. Once a muon is required to have matching tracks in the inner and outer detectors, the main source of background consists of charged hadrons that leave a signature in the inner silicon tracker while also penetrating through the hadronic calorimeter and creating hits in the muon chambers. Charged hadrons that penetrate the hadronic calorimeter and leave hits in the muon system will deposit significant energy in the calorimeters. Therefore, a calorimeter compatibility algorithm can be used to significantly reduce the number of charged pion fakes. However, calorimeter compatibility is not used in this analysis due to our uncertainty of the performance of such algorithms in the presence of high PU. The presence of punch-throughs often occur due to pions from the fragmentation of quarks and gluons. These punch-throughs can often be discriminated against by requiring isolation. Similarly, non-prompt muons from heavy flavor decays and decays in flights are expected to be within jets and can be discriminated against by imposing an isolation requirement. Muon identification is described in more detail in [?] and [?].

Isolated muons are required to have minimal energy from PF neutral and charged candidates

in a cone of $\Delta R = 0.4$ around the lepton trajectory. PF charged candidates considered in the calculation of isolation are required to be near the primary vertex. Isolation for muons is defined as:

$$I = \frac{\sum_i p_T^i}{p_T^\mu} \quad (8.1)$$

where the index i runs over PF neutral and charged candidates. Table 8.3 shows the complete list of for the “isMedium” μ identification criteria used in this analysis. In all channels, the identification and isolation used follows the POG recommended criteria.

Table 8.3: μ Identification

Cut
<pre> muon::isLooseMuon(recoMu) recoMu.innerTrack()-> validFraction() > 0.8 AND recoMu.globalTrack()-> normalizedChi2() < 3 recoMu.combinedQuality().chi2LocalPosition < 12 recoMu.combinedQuality().trkKink < 20 muon::segmentCompatibility(recoMu) > 0.303 OR muon::segmentCompatibility(recoMu) > 0.451 RelIso < 0.15 </pre>

8.4 Tau Reconstruction and Identification

The challenge in identifying hadronically decaying taus is discriminating against generic quark and gluon QCD jets which are produced with a cross-section several orders of magnitude larger. CMS has developed several algorithms to reconstruct and identify hadronically decaying taus based on Particle Flow (PF) objects. For this analysis, the tau POG recommended Hadron Plus Strips algorithm (HPS) is used. HPS makes use of PF jets as inputs to an algorithm that uses strips of clustered electromagnetic particles to reconstruct neutral pions. The electromagnetic strips (“neutral pions”) are combined with the charged hadrons within the PFJets to attempt to reconstruct the main tau decay modes outlined in Table 8.4.

Table 8.4: Reconstructed Tau Decay Modes

HPS Tau Decay Modes
Single Charged Hadron + Zero Strip
Single Charged Hadron + One Strip
Single Charged Hadron + Two Strips
Two Charged Hadrons
Three Hadrons

The single hadron plus zero strips decay mode attempts to reconstruct $\tau \rightarrow \nu\pi^\pm$ decays or $\tau \rightarrow \nu\pi^\pm\pi^0$ decays where the neutral pion has very low energy. The single hadron plus one or two electromagnetic strips attempts to reconstruct tau decays that produce neutral pions where the resulting neutral pion decays produce collinear photons. Similarly, the single hadron plus two strips mode attempts to reconstruct taus that decay via e.g. $\tau \rightarrow \nu\pi^\pm\pi^0$ where the neutral pion decays to well separated photons resulting in two electromagnetic strips. The three hadrons decay mode attempts to reconstruct tau decays that occur via $\rho(770)$ resonance. Although it is possible to recover signal in the two hadron decay mode (in the case of one of the three prongs being misidentified), this mode is not considered as its inclusion reduces discrimination performance and hurts the limit. In all cases, electromagnetic strips are required to have $E_T > 1$ GeV/c. Additionally, the particle flow charged hadrons are required to be compatible with a common vertex and have a net charge of $|q| = 1$.

In order to enforce the isolation requirement on the reconstructed tau, a region of size $R = 0.5$ around the tau decay mode direction is defined. Any PF candidates not used for the reconstruction of electromagnetic strips and charged hadrons not involved in the reconstruction of the tau decay modes are used to calculate isolation. The “Tight”, “Medium”, and/or “Loose” 3-hits isolation (with $\delta\beta$ corrections) working points are used.

In order to discriminate against muons, HPS taus are required to pass the lepton rejection discriminator which requires the lead track of the tau not be associated with a global muon signature. In order to discriminate against electrons, HPS taus are required to pass a MVA discriminator which uses the amount of HCAL energy associated to the tau with respect to the measured momentum

of the track (H/p). Additionally, the MVA discriminator considers the amount of electromagnetic energy in a narrow strip around the leading track with respect to the total electromagnetic energy of the tau. Finally, HPS taus must not reside in the ECAL cracks. In all channels, the identification and isolation used follows the Tau POG recommended criteria. The exact discriminator names and working points for each channel are listed and described in their respective sections.

8.4.1 Efficiency of Tau Identification discriminators

The efficiency of the τ_h ID discriminators used in the analysis are studied using Z'_{SSM} samples with $m(Z') = 2000$ GeV. For this purpose, we require the reconstructed τ_h to have $p_T > 45$ GeV and pseudorapidity $|\eta| < 2.1$. Further, reconstructed τ_h is matched to generator-level tau with $\Delta R(\tau_{reco}, \tau_{gen}) < 0.3$. The efficiency of the Decay Mode Finding (DMF) discriminator "DecayModeFinding" is found to be relatively flat at $\sim 80\%$ as shown in Figure 8.1. The individual efficiencies of anti-muon , anti-electron and isolation discriminators, relative to the DMF criterion, are shown in Figures 8.2– 8.4. The overall efficiency of τ_h ID selection used in this analysis is $\sim 55\%$. We use the VLoose working point of the anti-electron MVA5 discriminator as the tighter working points have poor performance (i.e. low efficiency which is also not "flat" vs. p_T). The relative flatness of the τ_h identification efficiency with p_T will also facilitate the use of $Z \rightarrow \tau\tau$ events as a "standard candle" for comparison with signal.

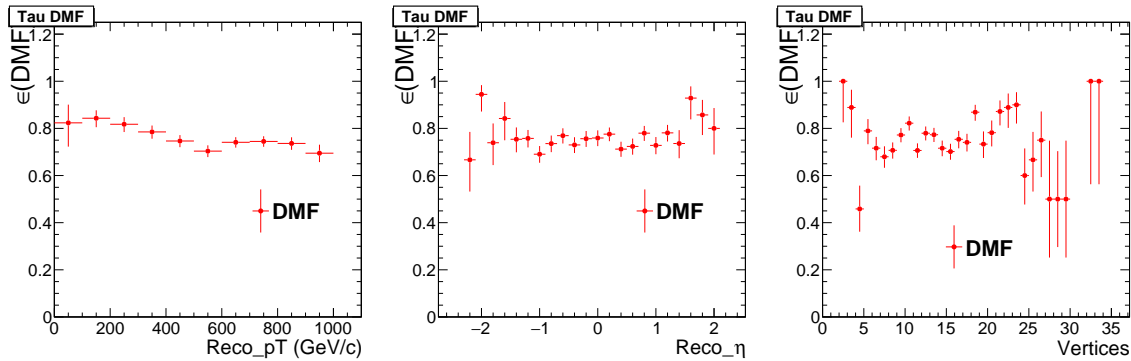


Figure 8.1: Decay Mode Finding efficiency as function of p_T , η , and number of vertices of generator-level taus

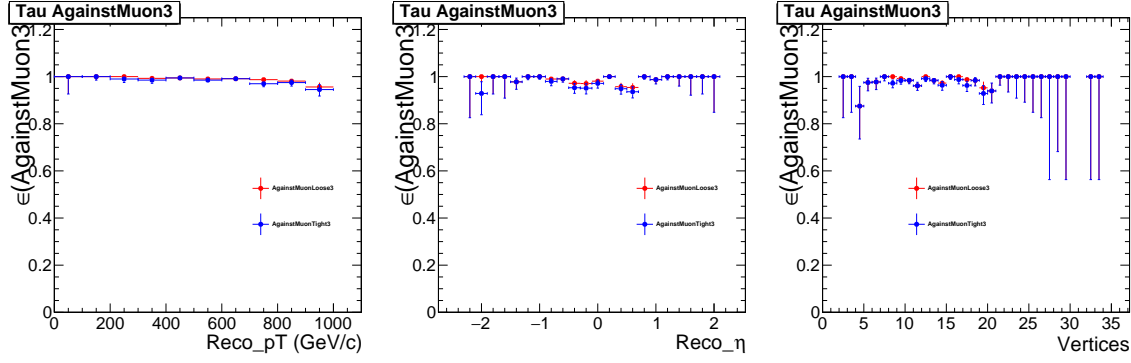


Figure 8.2: Efficiency of anti-muon discriminator (Loose3) as function of p_T , η , and number of vertices of generator-level taus

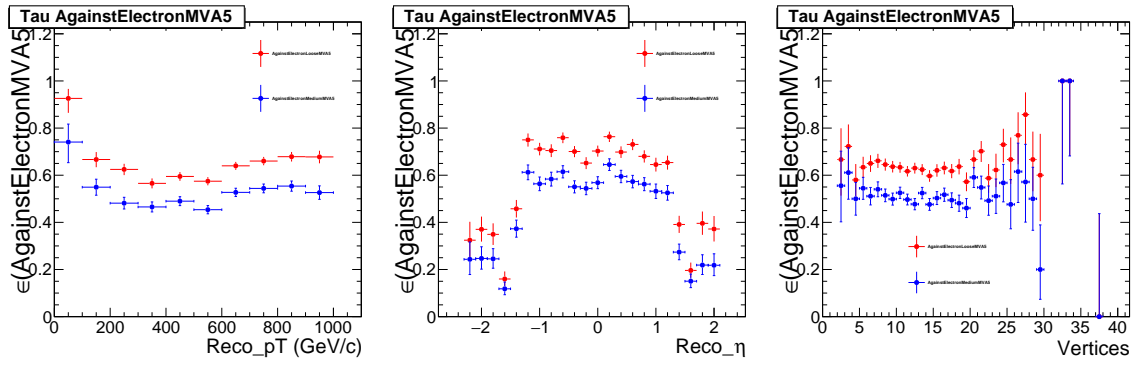


Figure 8.3: Efficiency of anti-electron discriminator (Loose/Medium MVA5) as function of p_T , η , and number of vertices of generator-level taus

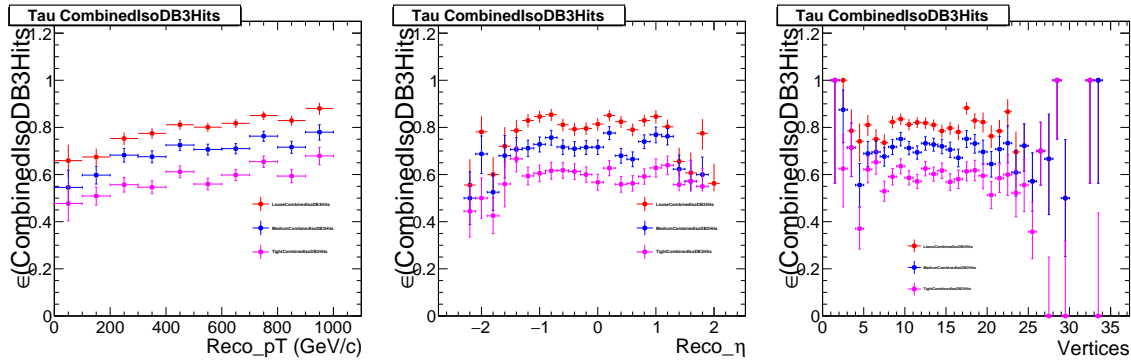


Figure 8.4: Efficiency of isolation discriminator ("CombinedIsoDB3Hits") as function of p_T , η , and number of vertices of generator-level taus

8.4.2 Tau Energy Scale and Resolution

Since the resolution and scale of our mass reconstruction depends on the effectiveness of the τ_h reconstruction, in this section we summarize our studies on τ_h response and resolution. We define the response as the difference between the transverse momentum of a reconstructed tau (that has passed all tau ID discriminators) and the transverse momentum of a generated tau that has been matched ($\Delta R < 0.3$) to the reconstructed tau. We can see from Figure 9 (right) that the response distribution contains a narrow gaussian like component in the bulk, in addition to a relatively long tail (compared to electrons and muons). While the tails become less substantial at high p_T , the gaussian-like bulk of the response distributions broaden at high p_T .

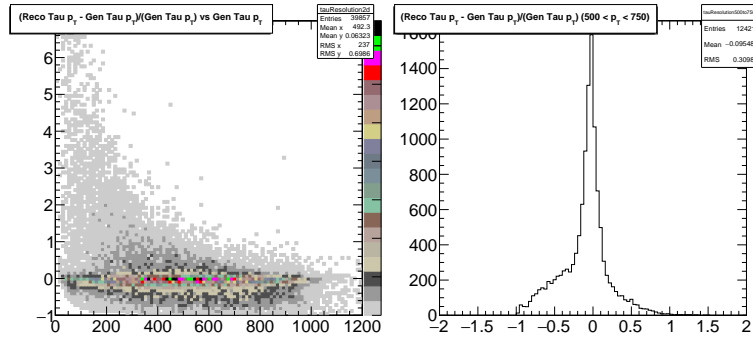


Figure 8.5: Energy response of reconstructed taus, raw and vs. generated tau p_T

8.5 E_T^{miss}

The presence of neutrinos in the $\tau\tau$ decays must be inferred from the imbalance of total momentum because they escape from the detector without producing any direct response. The magnitude of the negative vector sum of the visible transverse momentum is known as missing transverse energy, denoted E_T^{miss} .

Missing transverse energy is one of the most important observables for discriminating the signal events from background events which do not contain neutrinos, such as QCD multijet and DY $\rightarrow \mu\mu/\text{ee}$ events. Because there are many factors which may result in artificial E_T^{miss} , comprehen-

hensive studies of E_T^{miss} as measured using the CMS detector are performed [?]. We require events with $E_T^{miss} > 30$ GeV in all channels.

Finally, the standard and recommended “MET Filters” are utilized in this search.

8.6 Corrections for Pile-Up

Quantities such as \cancel{E}_T and isolation, where energy depositions are summed up over some range of the detector, can suffer large inefficiencies or systematic effects due to particles from pile-up interactions. Therefore, a simple and robust method must be employed to subtract off the contribution from secondary interactions. In the case of \cancel{E}_T , this is done by using the FastJet corrections to determine the density of PU on an event by event basis. For isolation, the recommended delta-beta corrections are applied. The recommended PU corrections have been included for all objects in all the channels.

We apply event-by-event the “official” pile-up weights ($\sigma = 69$ mb). Figure 8.6 shows the distributions of the number of reconstructed vertices, before and after applying the pile-up weights.

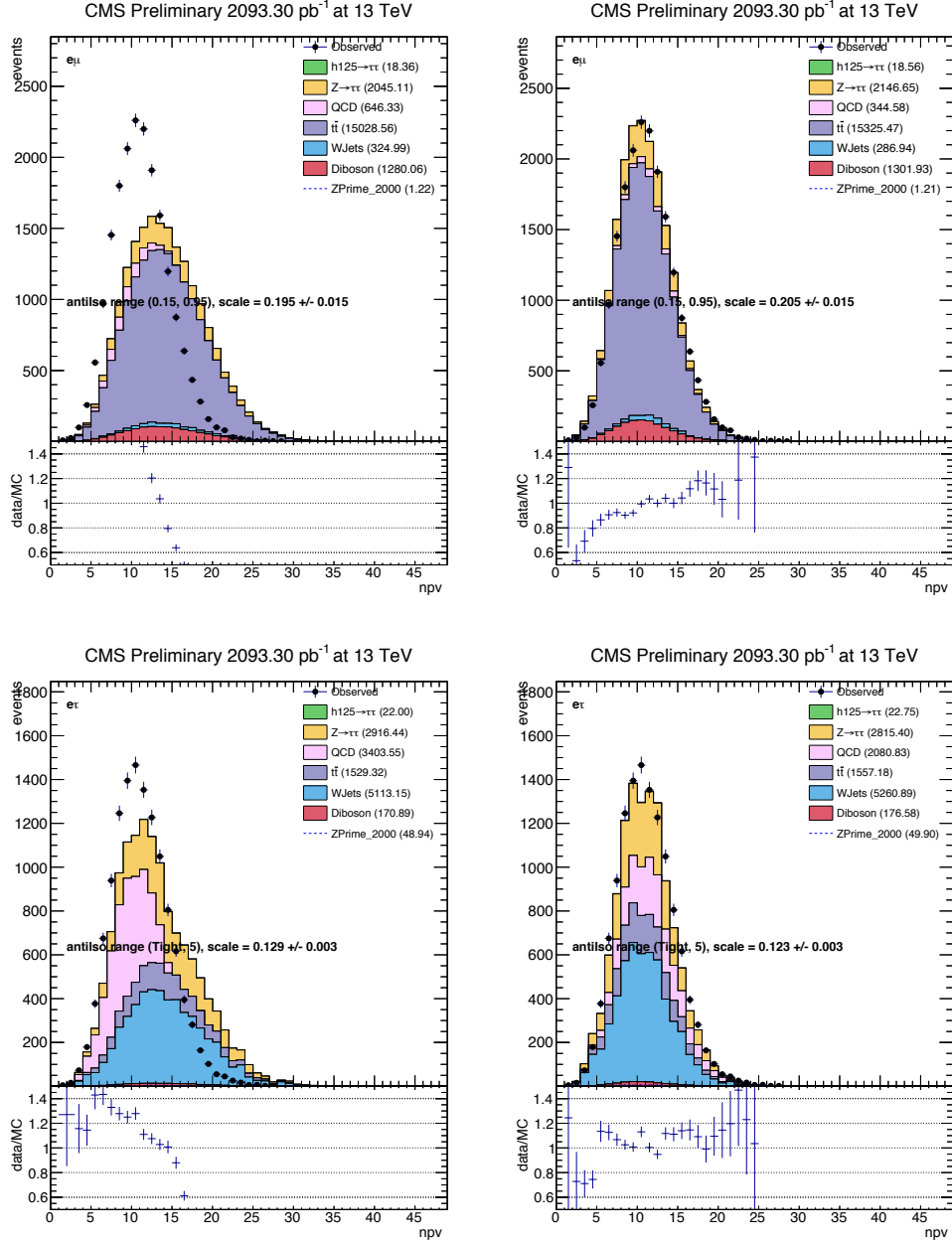


Figure 8.6: Distributions of the number of reconstructed primary vertices. Top: $e\mu$ channel. Bottom: $e\tau_h$ channel. Left: before reweighting. Right: after reweighting ("official" 69 mb). The ratios after reweighting become flattest at an "unofficial" value of 71 mb. The apparent substantial differences in the QCD "integrals" are artifacts of the plotting procedure, in which bins with negative contributions are zero-ed.